Experiment and Theory of the Broadband Absorption by a Tapered Hyperbolic Metamaterial Array

Jing Zhou,[‡] Alexander F. Kaplan,[‡] Long Chen, and L. Jay Guo*

Department of Electrical Engineering and Computer Science, University of Michigan, Ann Arbor, Michigan 48109, United States

S *Supporting Information*

ABSTRACT: A broadband absorber based on a tapered, alternating metal–dielectric multilayered structure was realized in the visible and IR range. The structure is fabricated by using a versatile method easily scalable to large areas by taking advantage of the line width reduction that occurs naturally in masked evaporation processes. The multilayered structure can be treated as a hyperbolic metamaterial (HMM), and the tapered structure can be regarded as a HMM waveguide with varying width. Light couples into the tapered structure most strongly at the mode cutoff position in the waveguide due to the hyperbolic dispersion and the phase matching condition. Resonant cavities are formed between the top of the tapered structure and the cutoff level, producing strong absorption peaks. These resonances are closely spaced spectrally due to the high k modes in HMM. Finally a broad absorption band is formed due to the broadening of the resonances from an array of coupled HMM tapered structures.

KEYWORDS: *hyperbolic metamaterial, broadband absorption, visible, IR, self-mask deposition*
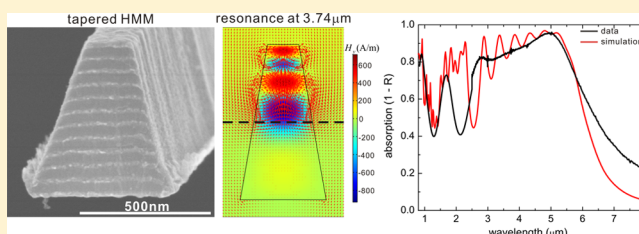
Broadband absorbers have received considerable interest due to their wide applications including IR cloaking,[1] photo- or thermal detection,[2-4] solar cells,[5-7] creating wider band thermal emitters, or harvesting waste heat for energy applications.[8] Some of these methods use materials such as carbon nanotubes to absorb light over a very large range of frequencies, but this involves structures that are micrometers thick, and there is little control over the spectral range. To create controlled absorption over a broad band, most scientists have focused on confining multiple plasmonic nanostructures with overlapping resonances into subwavelength pixels.[9-18] However, while these structures can create very high absorption through field confinement along with angle tolerance, only a finite amount of absorbers can be crammed into an area, limiting the bandwidth and complicating the fabrication procedure.

Anisotropic metamaterial structures have been proposed for broadband absorption.[19-22] One elegant design is a tapered structure of alternating metal–dielectric stacked layers, effectively trapping and absorbing transverse magnetic (TM) light over a wide range of frequencies.[23] This principle was first demonstrated in the microwave range.[24] Recently a microscopic version targeting the IR range was realized by focused ion beam.[25] However, an even smaller size targeting the visible–IR range and a scalable fabrication method toward realistic applications are still desired. From a theoretical perspective, the broadband absorption has been explained in terms of slow light characteristics in the tapered stack.[23,26] On the other hand, metal–dielectric multilayered structures have long been proposed as one type of hyperbolic metamaterial (HMM)[27-29] and proved by experiments.[30,31] Further, a

tapered pyramid made of metal–dielectric multilayers, very similar to the structure of the broadband absorber, was recently analyzed based on the hyperbolic dispersion of the metamaterial to explain its anomalous dependence of resonant frequency on cavity size.[32] This evidence naturally brings about the question of the connection between the multilayer broadband absorber and properties of HMMs in determining broadband absorption properties.

In this work, we first introduce a nanoimprint physical vapor deposition (PVD) method that experimentally realizes a tunable broadband absorber in the visible and IR range based on the tapered metal–dielectric multilayered structure. By taking advantage of the lateral growth of the deposited materials, the tapered shape is naturally formed when multistacks are directly deposited on a nanoimprinted resist template. Next we investigate the cause of the broadband absorption by treating the tapered metal–dielectric multi-layered structure as an HMM waveguide. We present a different understanding of the broadband absorption mechanism from the previous publications.[23-26] Due to the hyperbolic dispersion, there exists a cutoff position in this structure for each wavelength. Light is reflected at the cutoff level and interferes with the incident light to form subcavity resonances and produce absorption peaks. By simulating the absorption spectrum of a single HMM tapered waveguide under a plane wave incidence, we observed an absorption band consisting of many distinct peaks corresponding to the subcavity resonances. Strongest light coupling into the taper occurs near the cutoff

position where the propagation constant is the closest to the free space wave vector of incident light just outside the taper, therefore satisfying the phase matching condition. When made into a periodic structure, lateral coupling of the resonance modes between neighboring stacks occurs, which broadens the resonance peaks to form a broadband absorption.

■ RESULTS AND DISCUSSION

Experimental Realization of an HMM Broadband Absorber in the Visible and IR Range. We fabricated arrays of tapered metal−dielectric multilayered structures to target broadband absorption in the visible and IR range for TM waves (Figure 1). To begin, a reflective substrate (100 nm thick
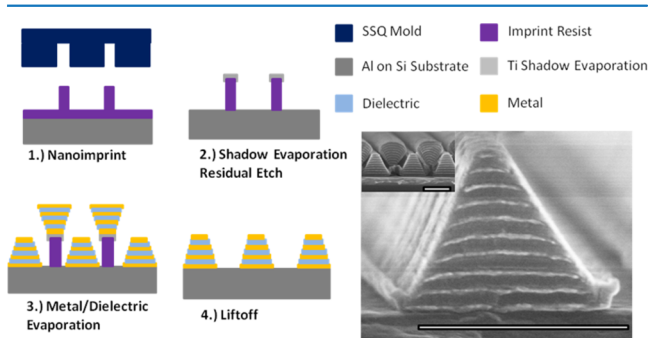

Figure 1. Fabrication process and SEM images for broadband absorber structure. (Left) Process flow for fabrication of tapered metal−dielectric structures using nanoimprint lithography. (Bottom right) SEM image of final 700 nm period structure with 9 stacks of Au−Al$_2$O$_3$ and (inset) prior to liftoff (step 3). Scale bar is 500 nm.

Al on a Si chip followed by a thin Cr adhesion layer) is coated with a polymer resist and imprinted under high temperature and pressure to create tall, narrow line width gratings (or a two-dimensional mesh if fabricating pillars). A thin Ti shadow deposition is then used to coat the tops of the gratings, and a reactive ion etch is performed to remove the residual resist. This shadow evaporation process prevents the thinning of the narrow resist lines while simultaneously determining the bottom width of our nanostructure.

In the next step, alternating metal and dielectric layers are deposited in succession until the desired height is achieved. Materials such as Au and Al were used for metals, while SiO$_2$, Al$_2$O$_3$, and Ge were used for dielectrics. As illustrated in Figure 1 step 3, the finite lateral growth on top of the resist masks deposition onto the substrate, creating a reduced line width with subsequent deposition. The amount of lateral growth and overall tapering of the structure has been shown to be dependent on a variety of factors including the directionality of the evaporated material and its ability to diffuse on the surface before sticking.[33] This means that parameters such as deposition rate, substrate temperature, and collimation of sources can be used to fine-tune the finished structure. Finally, an acetone liftoff is performed to remove the mask and the final nanostructure is created (scanning electron microscope (SEM) images are shown in the bottom right of Figure 1). Comparing with the recent demonstration based on FIB,[25] the advantages of the nanoimprint and liftoff approach are that they are parallel processes and can be easily scaled to large-area structures (typical samples used in our measurement are centimeter size). Furthermore, the nanoimprint−liftoff method can produce ultrasmall HMM tapered cavities (taper base smaller than 180

nm, period ∼220 nm) in order to target the visible region, shown in Figure 2d. However, with a usual Ga$^+$ ion FIB, it is difficult to define a period smaller than 300 nm for a depth of several hundred nanometers. In addition, due to the dielectrics in the multilayers, FIB could experience a charging effect, which could further reduce the resolution or make the sculpted faces rough. Ion mixing[34] or ion-induced heating could also blur the interface between the metal and the dielectric during FIB erosion.

Measurements in the IR range were conducted through a Fourier transform infrared (FTIR) spectroscopy tool. The measurements in the visible−near-IR range were conducted through a visible reflection setup with an integrated spectrometer and a spectroscopic ellipsometer. Finite element simulations were performed for comparison.

Figure 2b shows an array of 9-stack gratings using Au (∼20 nm)/Al$_2$O$_3$ (∼30 nm), targeting near-IR absorption, assuming the refractive index of Al$_2$O$_3$ to be ∼1.75. The array period is 700 nm. To shift the absorption band to the mid-IR, the same array period is used to create an 11-stack structure, shown in Figure 2c, replacing the dielectric by Ge due to its higher refractive index ($n \approx 4$). While the data and simulation show similar absorption ranges and peak values, simulations show peaks and valleys at shorter wavelengths that are not as strong in the experiment. This is due to an extra absorption loss caused by metal and the roughness in the fabricated device with respect to that ideally described by a Drude model. We found that by intentionally increasing the loss of metal in th esimulation, the peaks and valleys fade out (see Supporting Information). For absorption in a shorter wavelength range (visible), the multilayered taper is shrunk to less than 200 nm, as shown in the inset of Figure 2d. The tapered array has a 220 nm period and was fabricated using Al (∼20 nm)/SiO$_2$ (∼30 nm) stacks (SiO$_2$, index ∼1.45). In Figure 2d, the black curve uses data from a visible reflection setup with an integrated spectrometer instead of FTIR. The dashed blue curve is taken from angled data obtained using a spectroscopic ellipsometer with source and detector positioned at 45° from normal. These data are included to provide a wider spectral range than the visible reflection setup and demonstrate angle-tolerant absorption.

The alternating metal−dielectric multilayered structure with a period much smaller than the operating wavelength is described by effective medium theory as an HMM with an extremely anisotropic dielectric tensor $\vec{\varepsilon} = \text{diag}[\varepsilon_x, \varepsilon_y, \varepsilon_z]$, where $\varepsilon_x = \varepsilon_y = f\varepsilon_m + (1 - f)\varepsilon_d$ and $\varepsilon_z = \varepsilon_m\varepsilon_d/((1 - f)\varepsilon_m + f\varepsilon_d)$.[27] ε_m and ε_d are the permittivities of the metal and the dielectric; f is the fill ratio of the metal. The absorption spectrum of an array of Ag (20 nm)/Ge (30 nm) multilayered tapers (500 nm in bottom width, 182 nm in top width, and 900 nm in height) with a period of 700 nm is plotted in Figure 2e, as compared to its effective medium counterpart. Since the isofrequency contour (IFC) of the multilayered structure deviates from an ideal hyperbolic curve at large wave-numbers,[19,20] the spectrum is relatively blue-shifted with respect to that of the effective medium (see Supporting Information). Apart from that, the two spectra contain very similar absorption bands and peaks, confirming the validity of treating this structure as an HMM. In the following, we will investigate the physical mechanism responsible for the broadband absorption in the tapered array by using the effective medium approach.
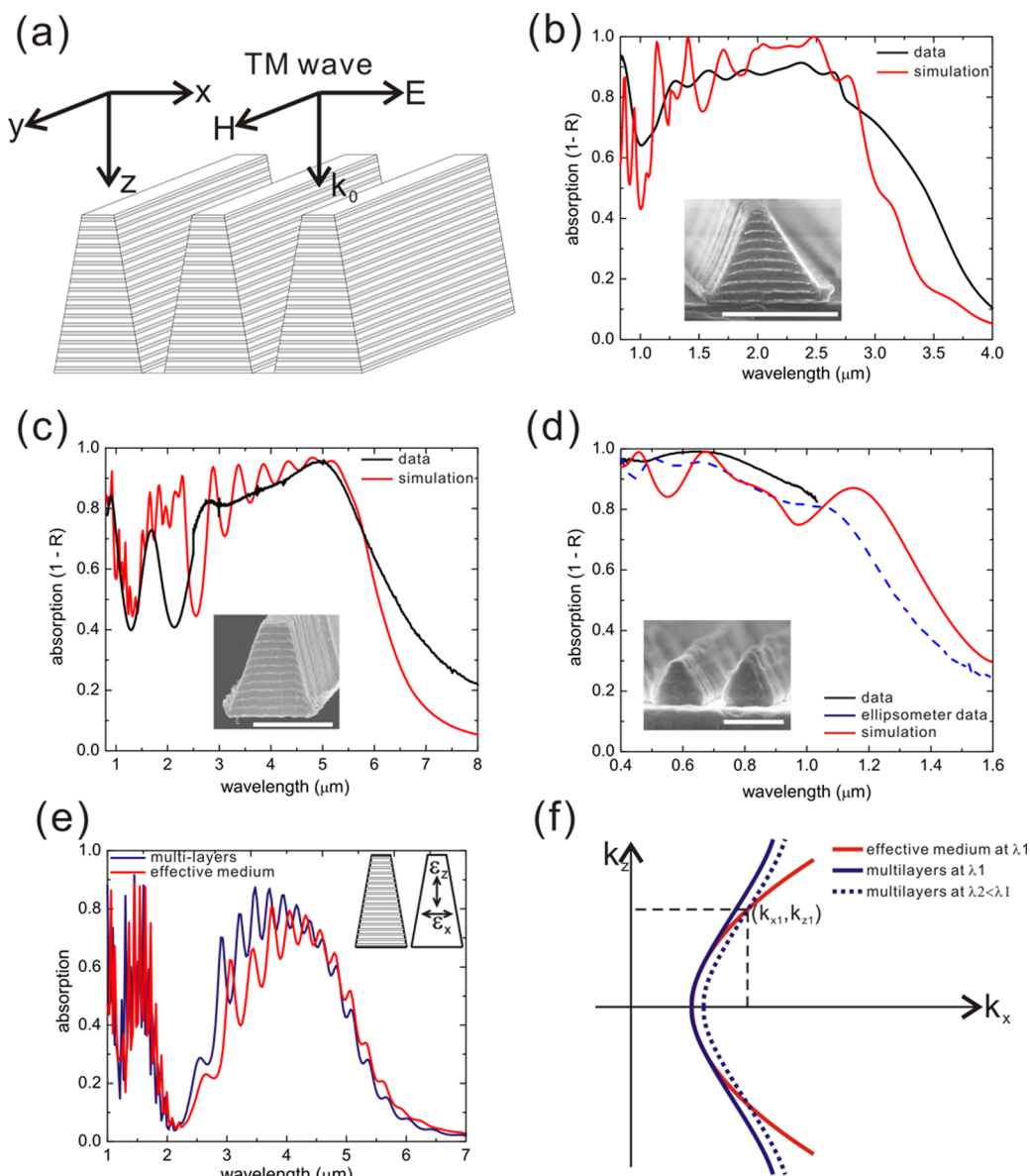
Figure 2. Experimental realization of the HMM broadband absorber targeting the visible and IR range. (a) Sketch of an array of metal−dielectric multilayered tapers under a TM wave incidence from the top. (b−d) Measured (black) and simulated (red) absorption curves for broadband absorbers with SEM images (inset): (b) 700 nm array period, 9-stack structure (Au−Al$_2$O$_3$) absorbing from ∼1.5 to 3 μm; (c) 700 nm array period, 11-stack structure (Au−Ge) absorbing from ∼2.5 to 6 μm; (d) 220 nm period, 3-stack structure (Al-SiO$_2$) absorbing from ∼0.4 to 1.2 μm, including angled data at 45° (dashed blue curve). Scale bars represent 500, 500, and 200 nm from (b) to (d). (e) Simulated absorption spectra of a multilayered structure and its effective medium counterpart under a TM wave incidence. The multilayered structure is an array of Ag (20 nm)/Ge (30 nm) multilayered, tapered HMM waveguides with a height of 900 nm, a tapering width from 500 nm at the bottom to 182 nm at the top, and a period of 700 nm. (f) Sketch of the isofrequency contour (IFC) of the multilayered structure (blue) compared with that of the effective medium (red). The dashed blue curve represents the IFC of the multilayered structure at a smaller wavelength.

Subcavity Formation in the HMM Taper. A unique characteristic of an HMM structure is that it supports propagation of waves with high wave vector k_x and k_z. Importantly, due to the hyperbolic IFC, k_x has a lower limit at the vertex of the hyperbolic curve, as shown in Figure 3a.

When the width of HMMs is confined in the x direction, light propagates in the z direction as a waveguide mode, with varying k_x and k_z depending on the waveguide width. On the basis of the simulated field pattern (Figure 3b), the TM$_0$ mode is excited inside the HMM tapered waveguide under a TM wave incident from the top. When propagating downward in the z direction, the mode experiences an increasing waveguide width so that k_x decreases due to reduced light confinement, as revealed by the successive lateral expansion of the light field. Because of the hyperbolic dispersion, k_z decreases as well, confirmed by the increased spatial oscillation period along the z direction. The evolution of the waveguide mode follows the hyperbolic IFC from the branch arm to the vertex, as shown in Figure 3a. The propagation as well as the evolution of the waveguide mode has to stop when it approaches the vertex. We will refer to this as the cutoff k_x in a tapered HMM waveguide.[23,26] There exists a corresponding cutoff waveguide width, where the power flow turns back. The cutoff k_x for our specific HMM structure [Ag (20 nm)/Ge (30 nm)] at the
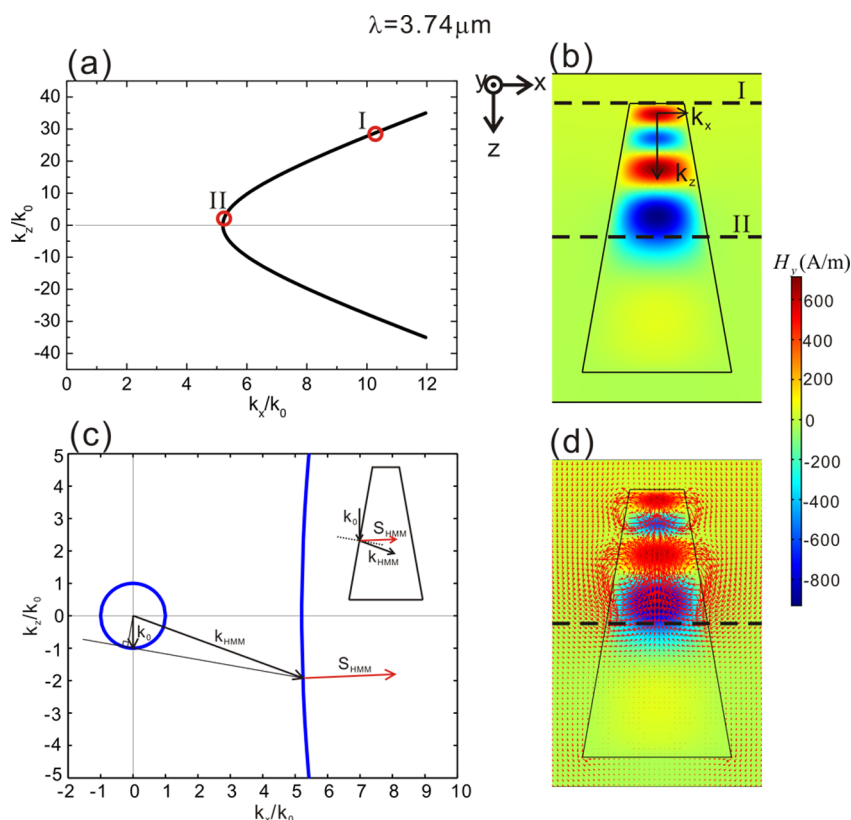
Figure 3. Light propagation in the HMM tapered waveguide and light coupling into the structure. (a) Hyperbolic IFC of the effective medium of the Ag (20 nm)/Ge (30 nm) multilayered structure at the wavelength of 3.74 μm. (b) Simulated H_y field distribution in the HMM taper under a TM wave incidence. The incident power flow is 2.5×10^5 W/m^2. The phase of the simulated field pattern is chosen to make the oscillating field at its maximum. (c) HMM IFC together with free space spherical IFC plotted with the lateral and vertical axes in equal proportion. Light refraction at the air/HMM interface is plotted based on phase matching (continuity in the tangential wavenumber). (d) Simulated time-averaged power flow distribution represented by arrows with a length proportional to the local magnitude.
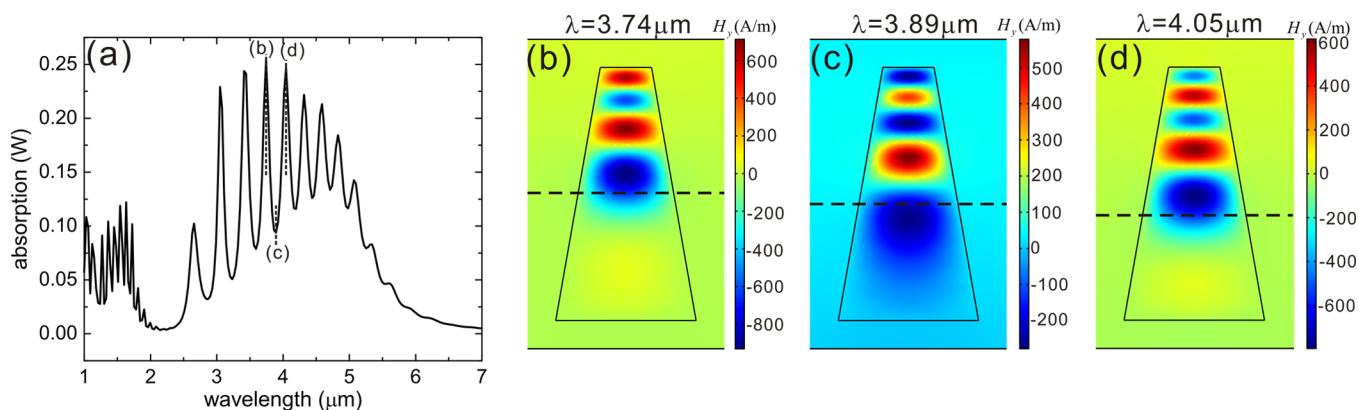

Figure 4. Subcavity resonances. (a) Absorption spectrum of the Ag (20 nm)/Ge (30 nm) HMM taper. (b)−(d) H_y field distribution at three adjacent resonant/nonresonant wavelengths (3.74, 3.89, and 4.05 μm). The dashed lines represent the cutoff level.

wavelength of 3.74 μm is calculated to be 5.31 times k_0 (free space wavenumber). We found that although the TM$_0$ mode is not allowed to propagate below the cutoff level, light power still could leak out as radiation modes or higher order modes (such as TM$_1$, TM$_3$, and so on). This is different from the previous theoretical analysis,[23,26] where the tapering is assumed to vary adiabatically such that the TM$_0$ mode cannot transfer into other modes except an allotrope that carries power back to the top. However, this adiabatic assumption is not valid in real fabricated samples. In our case, the impedance mismatch between the TM$_0$ mode above the cutoff level and those modes

below the cutoff level produces light reflection (see Supporting Information). At the top boundary, the propagation constant (k_z) is ~28 times bigger than k_0, leading to a nearly perfect reflection. Thus, a cavity is formed between the top boundary and the cutoff level, as manifested in Figure 3b. Due to the requirement of phase matching, the strongest light coupling occurs near the cutoff level, where k_z is the closest to k_0. This agrees with a simple picture depicted in Figure 3c of light refraction from air (represented by the circle) to an HMM medium (hyperbolic curve) at an angle where the refracted light mode corresponds to a point near the vertex of the
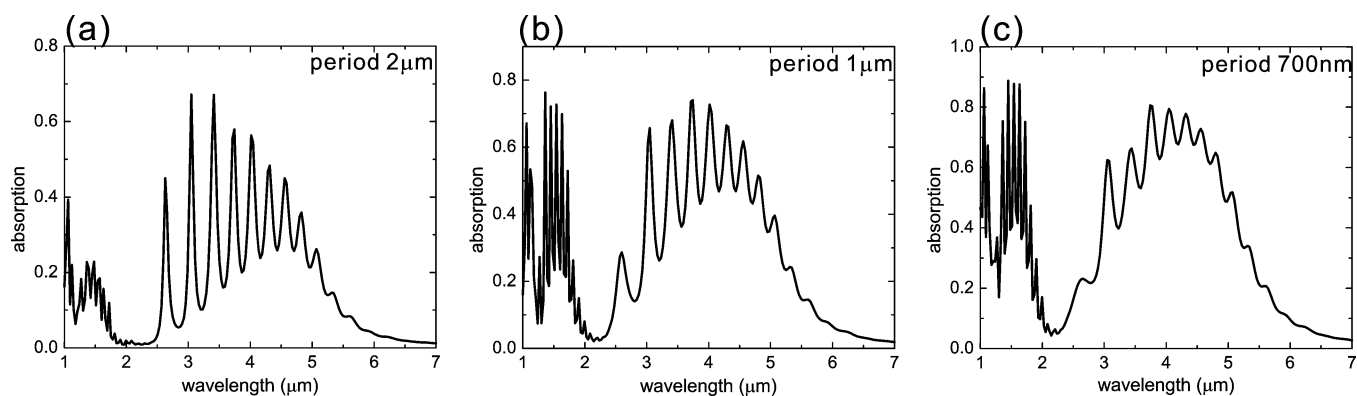
Figure 5. Absorption spectra at different array periods. (a–c) Absorption spectrum of the HMM tapers arrayed by a period of 2, 1, and 0.7 μm, respectively.
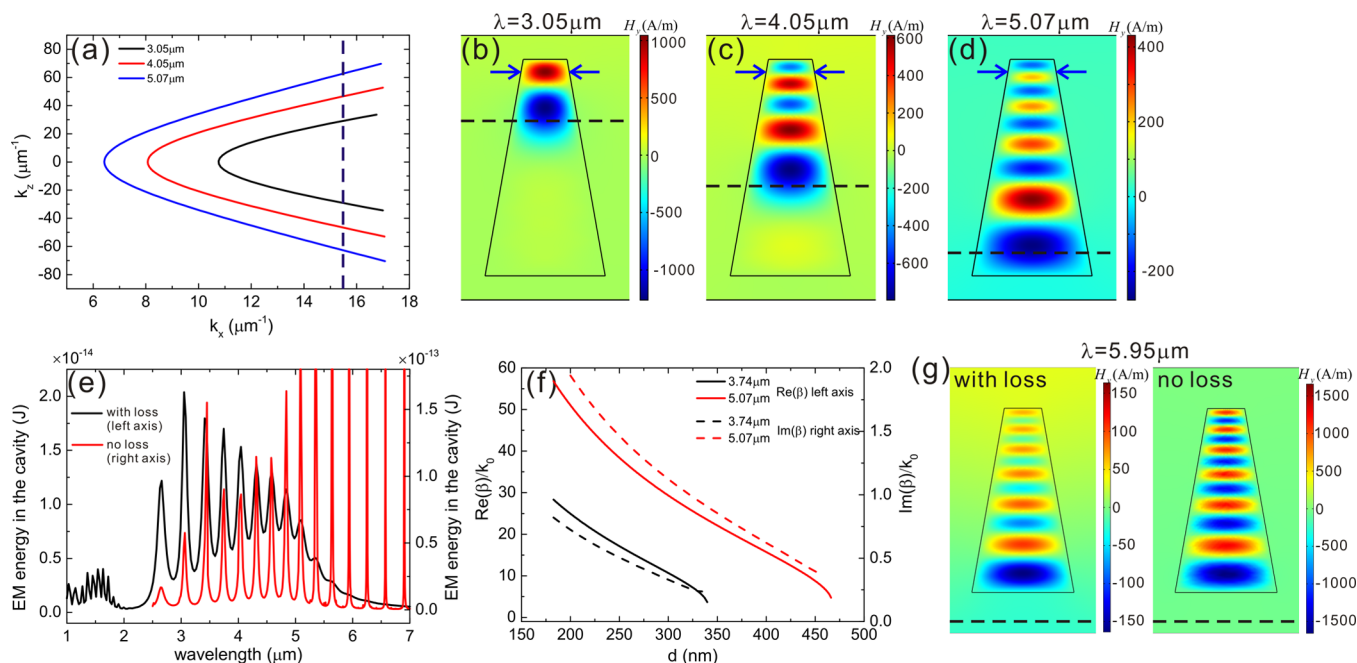

Figure 6. Wavelength dependence of the HMM waveguide mode and its influence on the absorption band. (a) Hyperbolic IFCs of the HMM at three wavelengths. The blue dashed line marks out the k_x corresponding to a certain width indicated by the paired arrows in (b)–(d). (b–d) Simulated H_y field distributions in the HMM taper under a TM plane wave incidence at three different wavelengths: 3.05, 4.05, and 5.07 μm. The TM wave with a power flow of 2.5×10^5 W/m^2 propagates downward from the top in the positive z direction. The dashed line denotes the cutoff level in each field pattern. (e) Electromagnetic energy stored inside the HMM taper versus wavelength. The black curve represents the HMM with a normal Ag. The red curve represents the lossless HMM with a zero-damping Ag. (f) Real (solid) and imaginary (dashed) parts of the effective index of the waveguide mode, as a function of waveguide width, at two wavelengths: 3.74 μm (black) and 5.07 μm (red). (g) H_y field distributions in the normal HMM and in the lossless HMM at a resonance (5.95 μm) where the cutoff level (black dashed line) exceeds the bottom boundary. The attenuation in the normal HMM and the consequent low intensity of the confined light field are observed.

hyperbolic IFC. In constructing this diagram, the conservation of transverse momentum of light is assumed as usual. The power flow follows the gradient direction of the IFC. The negative refraction of the power flow, which is a characteristic of HMM, makes the light power inside the tapered HMM propagate from the bottom to the top. The simulated time averaged power flow is represented by arrows with a length proportional to the local magnitude and confirms the strongest light coupling near the cutoff level and the power flow pointing to the top (Figure 3d).

Resonances in the Subcavity As Building Blocks of the Broadband Absorption. After light is coupled into the tapered HMM, it propagates in the waveguide mode and experiences reflection at the top boundary as well as the cutoff

level. A resonance is achieved by the constructive interference of the counter-propagating (or circulating) modes in the tapered waveguide, leading to a high field in the subcavity and an absorption peak. If constructive interference is not established, the light mode is in an off-resonance condition, which causes power to leak out and lowers the absorption. Three adjacent resonant/nonresonant wavelengths (3.74, 3.89, and 4.05 μm) are picked out from the absorption spectrum (Figure 4a).

In comparison to the two resonant cases (Figure 4b,d), where the light field is well confined between the top boundary and the cutoff level, the nonresonant case (Figure 4c) shows leakage of light field below the cutoff level. The resonance condition can be expressed as

$$2 \int_{I}^{II(\lambda)} k_z(z, \lambda) \, dz = 2n\pi \qquad (1)$$

where $k_z(z,\lambda)$ represents the propagation constant as a function of the position in the z-axis and the wavelength; the upper limit (II) and the lower limit (I) of the integral are the top boundary and the cutoff level, respectively. n is an arbitrary integer. Since k_z has very large values in the narrow area of the tapered HMM, a small change in the incident wavelength causes a big variation in phase accumulation. At the wavelength of 3.74 μm, there are two full cycles of oscillation inside the subcavity (Figure 4b), corresponding to an 8π phase accumulation in a round trip, fulfilling a resonance condition according to eq 1. The next resonance should have a 10π phase accumulation in a round trip. On the basis of the absorption spectrum (Figure 4a) and confirmed by the field pattern with two and a half cycles of oscillation in the subcavity (Figure 4d), this 10π resonance is found at a wavelength of 4.05 μm, which is only ~8% larger than 3.74 μm. This special characteristic of a HMM taper makes the resonances very close to each other in the spectrum, finally leading to the formation of a dense population of resonances with strong absorption peaks. When an array of HMM waveguides are separated by a subwavelength distance, resonances broaden and merge with each other, forming a broad absorption band that we observe in experiments. In principle, the formation of the absorption band is due to the intercoupling among the light modes in different tapered HMM structures, which is similar to the formation of electronic energy bands in a solid. This is evidenced by the absorption spectra of three tapered HMM arrays with different periods as shown in Figure 5a–c. A successive broadening and merging of the resonances are observed with decreasing period.

Wavelength Dependence of the HMM Waveguide Mode and Its Influence on the Absorption Band. Finally we investigate what determines the bandwidth of the absorption band in the tapered HMM. Since the k_x vertex of the hyperbolic IFC decreases with increasing wavelength (Figure 6a), the cutoff width increases correspondingly.

Thus, the cutoff level moves downward and the size of the subcavity expands, as shown in Figure 6b–d. Meanwhile, the propagation constant (k_z) of the waveguide mode is larger for longer wavelength, for any given k_x, as can be seen from the dispersion curves in Figure 6a. This trend is more clearly revealed by calculating the effective index $n_{eff} = k_z/k_0$ at different wavelengths, as shown in Figure 6f. As mentioned before, light coupling tends to occur at the position where k_z is close to k_0 as required by phase matching. With the increasing wavelength, k_z at all positions increases except for the area near the cutoff level, where k_z is still comparable to k_0, which allows maximum light coupling into the HMM waveguide. When the cutoff level moves out of the tapered HMM due to the increasing wavelength, light coupling occurs most efficiently near the bottom since the tapering shape guarantees the k_z at the bottom is the closest to k_0, although it could already be much larger than k_0. The scattering of light by the HMM tapered structure produces extra momentum, which makes up for the difference between k_0 and k_z so that light can couple into the cavity. However, the difference increases with the increasing wavelength, and thus the coupling efficiency reduces steadily. The same is true for light coupling out of the tapered HMM resonator, leading to a fast increase in the Q factor of the cavity. This is exhibited by the increase in Q factor of the resonances in an ideal HMM taper with no loss (red curve in

Figure 6e). The resonances get sharpened rapidly with the increasing wavelength starting from ~5.5 μm, where the cutoff level exceeds the bottom boundary. In reality, the metal loss induces a stronger attenuation at a higher k_z, as revealed by the increasing imaginary part of n_{eff} with wavelength (Figure 6f). Thus, with the increasing wavelength, especially after the cutoff level exceeds the bottom boundary, the increasing radiation Q makes light coupling more difficult and the increasing attenuation hinders the formation of resonances so that the light intensity inside the subcavity decreases, leading to the end of the absorption band.

■ CONCLUSION

HMM broadband absorbers targeting the visible and IR range were experimentally realized through a tapered, multilayered metal–dielectric structure. The structure is fabricated by using a nanoimprint-PVD method easily scalable to large areas by taking advantage of line width reduction that occurs naturally in evaporation processes through a patterned template. The absorption band was tuned from the visible to near-IR and to mid-IR range by changing the dielectric material or the size of the tapered HMM cavity. In a tapered HMM, there exists a cutoff width for each wavelength due to the hyperbolic dispersion. A subcavity is thus formed between the top boundary and the cutoff level. At a resonant wavelength, an intensified light field is built up inside the subcavity and an absorption peak is achieved. Due to the high k modes in HMM, the resonances are close to each other in the spectrum, making the building blocks of the broadband absorption. Due to the intercoupling between neighboring HMM waveguides, which are densely arrayed, the discrete resonances broaden and merge with each other, forming a band. Light coupling into the taper tends to occur at the position where k_z is close to k_0 as required by phase matching. With the increasing wavelength, especially after the cutoff level exceeds the bottom boundary, light coupling becomes more difficult and attenuation of the waveguide mode becomes more serious so that the light field is not effectively built up inside the cavity, leading to the end of the absorption band.

■ METHODS

The grating patterns were produced by a Nanonex NX-2000 imprinter. The multilayer structure was fabricated through electron beam physical vapor deposition. The finite element simulations were performed in Comsol Multiphysics. In our analysis, the model structure (Ag (20 nm)/Ge (30 nm) multilayers) has the permittivity of Ag following the Drude model, written as $\varepsilon_{Ag}(\omega) = 1 - \omega_p^2/(\omega^2 + i\omega\Gamma)$, where the bulk plasma frequency ω_p is chosen to be 9.013 eV and the damping frequency Γ is chosen to be 18 meV.[35] The permittivity of Ge is set to be a constant 4 throughout the studied wavelength range from 1 to 7 μm. The ideal HMM with no loss is achieved by setting the damping frequency Γ to zero. The simulation results in Figures 3–5 are based on a single HMM taper floating in free space.

■ ASSOCIATED CONTENT

ⓢ Supporting Information
Explanation of the blue-shifted spectrum of a multilayered structure with respect to the effective medium; further arguments for the subcavity resonances; study on angle tolerance of the broadband absorption; comparison between

two HMM cavities with different heights; and discussion about the difference between the simulated and the real spectrum. This material is available free of charge via the Internet at http://pubs.acs.org.

AUTHOR INFORMATION

Corresponding Author
*E-mail: guo@umich.edu.

Author Contributions
‡J. Zhou and A. F. Kaplan contributed equally.

Notes
The authors declare no competing financial interest.

ACKNOWLEDGMENTS

REFERENCES

(1) Shi, H.; Ok, J. G.; Baac, H. W.; Guo, L. J. Low density carbon nanotube forest as an index-matched and near perfect absorption coating. *Appl. Phys. Lett.* **2011**, *99*, 211103.

(2) Le Perchec, J.; Desieres, Y.; Espiau de Lamaestre, R. Plasmon-based photosensors comprising a very thin semiconducting region. *Appl. Phys. Lett.* **2009**, *94*, 181104.

(3) Nelms, N.; Dowson, J. Goldblack coating for thermal infrared detectors. *Sens. Actuators, A: Phys.* **2005**, *120*, 403−407.

(4) Theocharous, E.; Deshpande, R.; Dillon, A. C.; Lehman, J. Evaluation of a pyroelectric detector with a carbon multiwalled nanotube black coating in the infrared. *Appl. Opt.* **2006**, *45*, 1093−1097.

(5) Sondergaard, T.; Novikov, S. M.; Holmgaard, T.; Eriksen, R. L.; Beermann, J.; Han, Z.; Pedersen, K.; Bozhevolnyi, S. I. Plasmonic black gold by adiabatic nanofocusing and absorption of light in ultra-sharp convex grooves. *Nat. Commun.* **2012**, *3*, 969.

(6) Yu, Z.; Raman, A.; Fan, S. Fundamental limit of nanophotonic light trapping in solar cells. *Proc. Natl. Acad. Sci. U.S.A.* **2010**, *107*, 17491−17496.

(7) Leung, S.; Yu, M.; Lin, Q.; Kwon, K.; Ching, K.; Gu, L.; Yu, K.; Fan, Z. Efficient photon capturing with ordered three-dimensional nanowell arrays. *Nano Lett.* **2012**, *12*, 3682−3689.

(8) Coutts, T. J. A review of progress in thermophotovoltaic generation of electricity. *Renew. Sustain. Energy Rev.* **1999**, *3*, 77−184.

(9) Cui, Y.; Xu, J.; Fung, K. H.; Jin, Y.; Kumar, A.; He, S.; Fang, N. X. A thin film broadband absorber based on multi-sized nanoantennas. *Appl. Phys. Lett.* **2011**, *99*, 253101.

(10) Ye, Y. Q.; Jin, Y.; He, S. Omnidirectional, polarization-insensitive and broadband thin absorber in the terahertz regime. *J. Opt. Soc. Am. B* **2010**, *27*, 498−504.

(11) Bouchon, P.; Koechlin, C.; Pardo, F.; Haïdar, R.; Pelouard, J. L. Wideband omnidirectional infrared absorber with a patchwork of plasmonic nanoantennas. *Opt. Lett.* **2012**, *37*, 1038−1040.

(12) Koechlin, C.; Bouchon, P.; Pardo, F.; Jaeck, J.; Lafosse, X.; Pelouard, J.; Haidar, R. Total routing and absorption of photons in dual color plasmonic antennas. *Appl. Phys. Lett.* **2011**, *99*, 241104.

(13) Hendrickson, J.; Guo, J.; Zhang, B.; Buckwald, W.; Soref, R. Wideband perfect light absorber at midwave infrared using multiplexed metal structures. *Opt. Lett.* **2012**, *37*, 371−373.

(14) Cheng, C.; Abbas, M. N.; Chiu, C.; Lai, K.; Shih, M.; Chang, Y. Wide-angle polarization independent infrared broadband absorbers based on metallic multi-sized disk arrays. *Opt. Express* **2012**, *20*, 10376−10381.

(15) Jiang, Z. H.; Yun, S.; Toor, F.; Werner, D. H.; Mayer, T. S. Conformal dual-band near-perfectly absorbing mid-infrared metamaterial coating. *ACS Nano* **2011**, *5*, 4641−4647.

(16) Wen, Q. Y.; Zhang, H. W.; Xie, Y. S.; Yang, Q. H.; Liu, Y. L. Dual band terahertz metamaterial absorber: Design, fabrication, and characterization. *Appl. Phys. Lett.* **2009**, *95*, 241111.

(17) Tao, H.; Bingham, C. M.; Pilon, D.; Fan, K.; Strikwerda, A. C.; Shrekenhamer, D.; Padilla, W. J.; Zhang, X.; Averitt, R. D. A dual band terahertz metamaterial absorber. *J. Phys. D: Appl. Phys.* **2010**, *43*, 225102.

(18) Li, H.; Yuan, L. H.; Zhou, B.; Shen, X. P.; Cheng, Q.; Cui, T. J. Ultrathin multiband gigahertz metamaterial absorbers. *J. Appl. Phys.* **2011**, *110*, 014909.

(19) Yang, J.; Hu, X.; Li, X.; Liu, Z.; Liang, Z.; Jiang, X.; Zi, J. Broadband absorption enhancement in anisotropic metamaterials by mirror reflections. *Phys. Rev. B* **2009**, *80*, 125103.

(20) Yang, J.; Hu, X.; Li, X.; Liu, Z.; Jiang, X.; Zi, J. Cancellation of reflection and transmission at metamaterial surfaces. *Opt. Lett.* **2010**, *35*, 16−18.

(21) He, S.; He, Y.; Jin, Y. Revealing the truth about 'trapped rainbow' storage of light in metamaterials. *Sci. Rep.* **2012**, *2*, 583.

(22) Tsakmakidis, K. L.; Boardman, A. D.; Hess, O. 'Trapped rainbow' storage of light in metamaterials. *Nature* **2007**, *450*, 397−401.

(23) Cui, Y.; Fung, K. H.; Xu, J.; Ma, H.; Jin, Y.; He, S.; Fang, N. X. Ultrabroadband light absorption by a sawtooth anisotropic metamaterial slab. *Nano Lett.* **2012**, *12*, 1443−1447.

(24) Ding, F.; Cui, Y.; Ge, X.; Jin, Y.; He, S. Ultra-broadband microwave metamaterial absorber. *Appl. Phys. Lett.* **2012**, *100*, 103506.

(25) Ji, D.; Song, H.; Zeng, X.; Hu, H.; Liu, K.; Zhang, N.; Gan, Q. Broadband absorption engineering of hyperbolic metafilm patterns. *Sci. Rep.* **2014**, *4*, 4498.

(26) Hu, H.; Ji, D.; Zeng, X.; Liu, K.; Gan, Q. Rainbow trapping in hyperbolic metamaterial waveguide. *Sci. Rep.* **2013**, *3*, 1249.

(27) Cortes, C. L.; Newman, W.; Molesky, S.; Jacob, Z. Quantum nanophotonics using hyperbolic metamaterials. *J. Opt.* **2012**, *14*, 063001.

(28) Cai, W.; Shalaev, V. *Optical Metamaterials: Fundamentals and Applications*; Springer: Berlin, 2009; pp 11−36.

(29) Jacob, Z.; Kim, J.; Naik, G. V.; Boltasseva, A.; Narimanov, E. E.; Shalaev, V. M. Engineering photonic density of states using metamaterials. *Appl. Phys. B: Lasers Opt.* **2010**, *100*, 215−218.

(30) Krishnamoorthy, H. N. S.; Jacob, Z.; Narimanov, E.; Kretzschmar, I.; Menon, V. M. Topological transitions in metamaterials. *Science* **2012**, *336*, 205−209.

(31) Ni, X.; Naik, G. V.; Kildishev, A. V.; Barnakov, Y.; Boltasseva, A.; Shalaev, V. M. Effect of metallic and hyperbolic metamaterial surfaces on electric and magnetic dipole emission transitions. *Appl. Phys. B: Lasers Opt.* **2011**, *103*, 553−558.

(32) Yang, X.; Yao, J.; Rho, J.; Yin, X.; Zhang, X. Experimental realization of three-dimensional indefinite cavities at the nanoscale with anomalous scaling laws. *Nat. Photonics* **2012**, *6*, 450−454.

(33) Chanda, D.; Shigeta, K.; Gupta, S.; Cain, T.; Carlson, A.; Mihi, A.; Baca, A. J.; Bogart, G. R.; Braun, P.; Rogers, J. A. Large-area flexible 3D optical negative index metamaterial formed by nanotransfer printing. *Nat. Nanotechnol.* **2011**, *6*, 402−407.

(34) Nastasi, M.; Mayer, J. W., Ion-Induced Atomic Intermixing at the Interface: Ion Beam Mixing. In *Ion Implantation and Synthesis of Materials*; Springer: Berlin, 2006; pp 179−192.

(35) Ordal, M.; Bell, R.; Alexander, R.; Long, L.; Querry, M. Optical-Properties of 14 Metals in the Infrared and Far Infrared - Al, Co, Cu, Au, Fe, Pb, Mo, Ni, Pd, Pt, Ag, Ti, V, and W. *Appl. Opt.* **1985**, *24*, 4493−4499.